14 Introduction to Scanning Tunneling Spectroscopy of Correlated Materials

Christian Hess
IFW Dresden
Helmholtzstraße 20, 01069 Dresden, Germany

Contents

1 Introduction **2**

2 Basics **2**
2.1 Methods 2
2.2 Quasiparticle interference 5

3 Iron-based superconductors **7**
3.1 Gap spectroscopy 8
3.2 Quasiparticle interference 13

4 Cuprate superconductors **21**
4.1 Quasiparticle interference and the octet-model 21
4.2 Nanoscale electronic order 23

5 Conclusion **23**

E. Pavarini, E. Koch, J. van den Brink, and G. Sawatzky (eds.)
Quantum Materials: Experiments and Theory
Modeling and Simulation Vol. 6
Forschungszentrum Jülich, 2016, ISBN 978-3-95806-159-0
http://www.cond-mat.de/events/correl16

1 Introduction

During the last 15–20 years, scanning tunneling microscopy and spectroscopy (STM/STS) has developed into an indispensable experimental tool of modern condensed matter physics. This method provides real-space dependent spectroscopic information of a solid's surface at the atomic scale. It is thus capable to directly observe quantum mechanical effects, which in turn provide new insight into the properties of a solid, which includes, remarkably, even momentum-resolved information on electronic states.
The purpose of this lecture is to convey the main experimental concepts of STM/STS for the research on correlated materials. Thereby, it cannot and does not aim at comprehensively covering STM/STS work on all kinds of different material classes of correlated systems. The focus will be specifically on unconventional superconductors, which are, among the electronically correlated materials, the most prominent ones where STM/STS has been successfully used, providing new ground-breaking insights. After a more general introduction to the experiment itself, the lecture will first specifically address the unconventional superconductor LiFeAs, for which comprehensive STM/STS data of high quality exist and which is still a matter of ongoing research. This will be complemented by briefly summarizing fundamental work on cuprate superconductors. It can be expected readers who digest the thereby introduced techniques and concepts will be able to easily access other existing and future work on correlated materials with STM/STS.

2 Basics

2.1 Methods

We consider an atomically sharp metallic tip that is brought into close distance (a few Ångstroms) to the surface of a solid, i.e. the sample which we would like to investigate. In this situation, electrons tunnel from the tip to the sample and vice versa. If both are at the same electrochemical potential the net current will be zero. A finite net tunneling current will, however, arise when we apply an electrical bias voltage U_{bias} between the tip and the sample [1–3]

$$I = A|M|^2 N_0 \int_{-\infty}^{\infty} \rho_s(E)[f(E) - f(E - eU_{\mathrm{bias}})]\, dE\,, \tag{1}$$

with A a constant of proportionality, M the tunneling matrix element, and f the Fermi distribution function. N_0 and ρ_s are the density of states (DOS) of the tip and the local density of states (LDOS) of the sample at the position of the tip, respectively. Note that already in Eq. (1) significant approximations have been made which we will assume to be valid throughout this chapter unless stated otherwise: Both N_0 and $|M|^2$ are assumed to be energy independent, and thus can be written in front of the integral. Approximate energy independence can be achieved for the former by using an appropriate tip material. For the latter it is reasonably valid at small U_{bias} and for sufficiently simple electronic structure (see e.g. [4] for a more elaborate discussion).

It has been shown further – and this is crucial for the exploitation of the tunneling current for microscopy – that the tunneling matrix element decays exponentially with increasing distance d between the tip and the sample [2, 3], viz. $I \propto e^{-2\kappa d}$, where κ depends on the work functions of the sample and the tip. This means the well known exponentially decaying tunneling probability for one-dimensional electron tunneling depending on the width of the vacuum barrier is recovered. The other crucial finding from Eq. (1) is that, at temperature $T = 0$, the tunneling current I is proportional to the LDOS of the sample integrated between the Fermi level ϵ_F and $\epsilon_F + eU_{\rm bias}$. At finite temperature, this energy interval is, of course, broadened through the Fermi functions.

2.1.1 Scanning tunneling microscopy (STM)

In a scanning tunneling microscope, the relative position of the tunneling tip to the sample can be controlled in the three spatial dimensions x, y parallel and z perpendicular to the sample's surface, where nowadays a precision in the picometer range can be achieved (see e.g. [4, 5] for details on the technical realization). This opens up a plethora of possibilities for probing the surface of a sample. A fundamentally important measurement mode is scanning tunneling microscopy (STM), i.e., a high-resolution measurement of the surface topography. A very important way to do this (among others) is the so-called constant-current topography mode: The actuator for tip motion along the z-direction is connected to a feed-back loop that measures the tunneling current I and maintains it constant during scanning the tip in the (x, y)-plane by appropriately adjusting the z-position of the tip which regulates the distance d between tip and sample. Inspection of Eq. (1) tells us that the resulting data set $z(x, y)$ describes a plane of constant integrated LDOS of the sample (within ϵ_F and $\epsilon_F + eU_{\rm bias}$). Due to the very high lateral and vertical resolution in STM, it is possible to resolve even the atomic corrugation of a surface. Fig. 1 depicts representative data taken from 2H-$NbSe_2$. This compound exhibits a charge density wave (CDW) at low temperature, yielding a 3×3 superlattice [6]. The topographic STM data in Fig. 1 very clearly reveal this superstructure [8], which highlights that the STM is susceptible to the spatial modulations of the electronic LDOS (which in the present example is generated by the CDW). Further below, we shall see more examples of spatial modulations in the LDOS which can be detected in STM.

2.1.2 Scanning tunneling spectroscopy (STS)

Eq. (1) implies that through measuring the tunneling current as a function of $U_{\rm bias}$, the LDOS of the sample at a fixed position of the tip, i.e. $\rho_s(E)$ with $E = eU_{\rm bias}$, can be accessed. In the experiments, the differential conductance

$$\left.\frac{dI}{dU}\right|_{U=U_{\rm bias}} \propto \int_{-\infty}^{\infty} \rho_s(E) \left.\frac{\partial f(E-eU)}{\partial(eU)}\right|_{U=U_{\rm bias}} dE, \tag{2}$$

is evaluated, either by numerical derivation or by directly measuring it using a lock-in amplifier (see [4, 5] for details). Eq. (2) describes the convolution of ρ_s with the voltage derivative of the

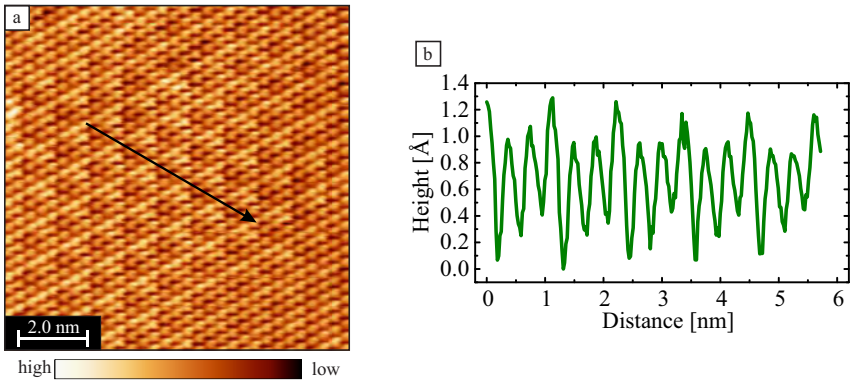

Fig. 1: *(a) Constant current topographic image of 2H-$NbSe_2$ in a field of view of* $10\ nm \times 10\ nm$*,* $U_{\rm bias} = -200$ *mV,* $I = 0.7$ *nA,* $T = 10$ *K. The topography shows the atomic corrugation of the topmost layer of Se atoms, and reveals the CDW with a periodicity of* $3a \times 3a$ *with the lattice constant* $a = 0.0345$ *nm [7]. (b) Line section taken along the arrow. Image and graph taken from [8].*

Fermi distribution function which is a bell-shaped curve centered around $U_{\rm bias}$ with a FWHM of about $3.5\, k_B T$. Thus, the spectroscopic resolution in energy ΔE is inevitably thermally broadened. Scanning tunneling spectroscopy (STS) with high energy resolution therefore requires measurements at very low temperatures. Typical values for ΔE at the cryogenically relevant temperatures 300 mK and 4.2 K are 90 μeV and 1.3 meV, respectively.

In a scanning tunneling microscope, spectroscopic measurements of the differential conductance dI/dU can be performed as a function of the spatial tip position, which provides the unique possibility to map out the energy dependent LDOS as a function of the (x, y) position. The resulting data for $\rho_s(E, x, y)$ are often false-color plotted in a two-dimensional fashion as a function of (x, y) at a fixed $E = eU_{\rm bias}$, a technique often called *Spectroscopic Imaging (SI-STM).* The resulting images provide valuable information about the energy dependence of the spatial modulations of the LDOS. Fig. 2 shows an example for the spatially dependent LDOS due to the CDW in 2H-$NbSe_2$ at two selected energies. The data reveal a much stronger impact of the CDW on the LDOS at $U_{\rm bias} = -100$ mV than at $U_{\rm bias} = +100$ mV [8].

One way to acquire the data is to measure dI/dU at a fixed $U_{\rm bias}$, while scanning a surface of interest as a function of (x, y). Here, a small modulation voltage $U_{\rm mod}$ is added to $U_{\rm bias}$, and $dI/dU|_{U_{\rm bias}}$ is measured directly with a lock-in amplifier. This method (sometimes called dI/dU*-imaging*) has the advantage that a spatially highly resolved dI/dU-map can be relatively quickly recorded together with a topographic map (in the order of minutes to a few hours), thus posing only moderate constraints on the stability of the used microscope. However, the data contain dI/dU information only for one specific energy E. Therefore, in order to acquire a much more comprehensive data set of $\rho_s(E, x, y)$ at a larger set of energy values, a different measurement protocol is used: The surface of interest is scanned topographically where the position of the tip is kept fixed (with feed-back loop switched off) at a grid of (x, y) positions, and at each of these positions the differential conductance is measured as a function of $U_{\rm bias}$. This technique typically yields a large and comprehensive data set which allows to visualize,

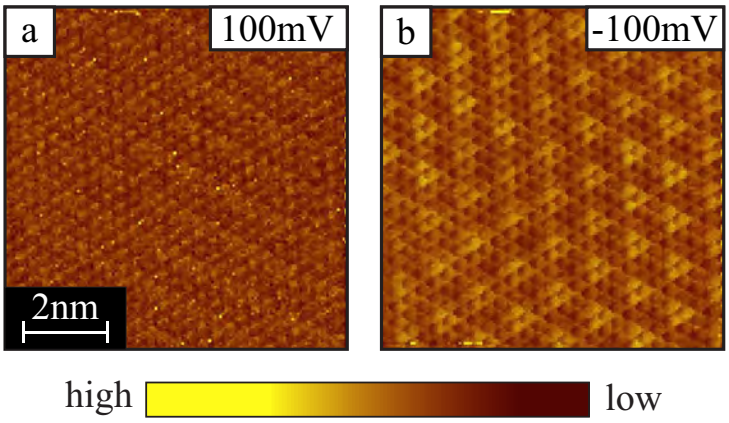

Fig. 2: 128×128 *spectroscopic* dI/dU *maps in a field of view of* $8\ nm \times 8\ nm$ *of 2H-NbSe*$_2$ *at stabilization conditions* $U_{\mathrm{bias}} = 200$ *mV,* $I = 0.7$ *nA,* $T = 10$ *K, RMS lock-in excitation* $U_{\mathrm{mod}} = 6$ *mV,* $t_{\mathrm{map}} = 16.5$ *h, spectra measured from 100 mV to* -100 *mV; (a)* dI/dU *spectroscopic map at 100 mV; (b)* dI/dU *spectroscopic map for* -100 *mV. The CDW pattern is hardly visible at 100 mV but clearly observable at* -100 *mV. The atomic structure is prominent at both voltages. Images taken from [8].*

e.g., the spatial dependence of $\rho_s(E, x, y)$ at deliberate E values. This is particularly important if the details of the energy dependence of the phenomenon under scrutiny are unknown, as is often the case for the case of correlated materials as well. The only drawback with respect to the dI/dU-imaging is the relatively long measurement duration of several days[1] for this often called *full-spectroscopy* mapping. Such long measurement times require perfect stability of the microscope with atomic fidelity during the whole measurement.

2.2 Quasiparticle interference

The screening of a point-like impurity in a metal results in an oscillating charge density as a function of distance from the impurity, known as Friedel oscillation [9]. The observation of such oscillations emerging from impurity atoms or atomic step edges [10, 11] has been one of the early groundbreaking discoveries of STM. Fig. 3 shows corresponding data for the Cu(111) surface, which possesses a two-dimensional surface state with a band minimum at about -0.44 meV [10] (see also Fig. 4c for the Fermi surface). The topography measurement in Fig. 3a very clearly reveals wave-like modulations of the integrated LDOS at the step edges, and in addition the signatures of point-like impurities on the terraces with radially emerging wave-like patterns. The latter can be observed even better in Fig. 4a. For modeling the energy-dependent modulation of the LDOS, typically a scattering scenario is invoked, where an electron is back-scattered at the step edge or the point-impurity, resulting in the wave interference of the incoming and the outgoing electrons, and thus a standing electronic wave pattern. For the step edges one finds [12, 10]

$$\rho_s(E, x) \propto \{1 - J_0[2q(E)x]\}, \tag{3}$$

[1] Simple math tells us that if a single full-spectroscopy dI/dU curve requires about 10 s measurement time, a spatially highly resolved data set at e.g. 256×256 pixels requires about 7.5 days of total measurement time.

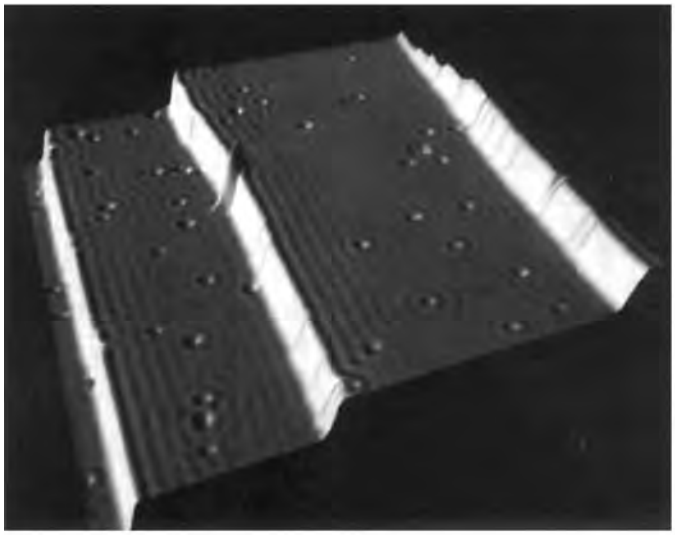

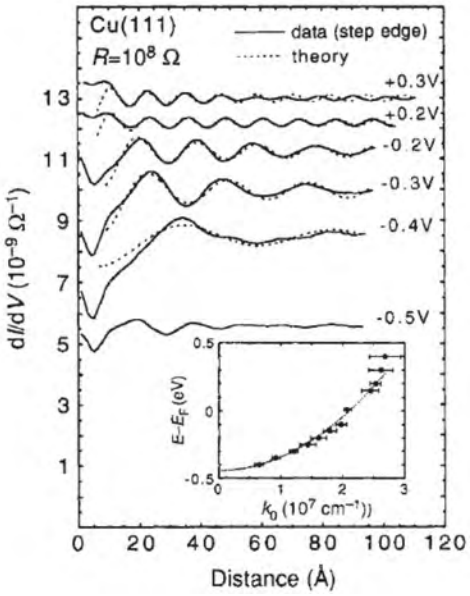

Fig. 3: *Left: constant-current* $500\ \text{Å} \times 500\ \text{Å}$ *image of the Cu(111) surface (*$U_{\text{bias}} = 0.1$ *V,* $I = 1.0$ *nA). Three monatomic steps and about 50 point defects are visible. Spatial oscillations with a periodicity of* ~ 15 *Å are clearly evident. The vertical scale has been greatly exaggerated to display the spatial oscillations more clearly. Right: Solid lines: spatial dependence of* dI/dU*, measured as a function of distance from step edge at different* U_{bias}*. Zero distance corresponds to the lower edge of the step. Dashed lines: theoretical fits of Eq.* (3) *to the data. Curves have been shifted vertically for viewing. Inset: experimental surface state dispersion, obtained from fits of Eq.* (3) *to the* dI/dU *linescan data. The dashed line is a parabolic fit used to extract the surface state effective mass and band edge. Figures taken from [10].*

with the energy E, the distance from the step edge x, and q the length of energy dependent wave vector of the modulation. J_0 is the zeroth-order Bessel function. For the point-like impurities the result is [12, 10]

$$\rho_s(E, r) \propto 1 + \frac{2}{\pi q r}\left[\cos^2\left(qr - \frac{\pi}{4} + \eta_0\right) - \cos^2\left(qr - \frac{\pi}{4}\right)\right], \tag{4}$$

where r is the radial distance from the impurity and η_0 a phase shift.
Fig. 3b shows $dI/dU|_{U_{\text{bias}}}$ measurements as a function of the distance x from the step edge at various energies $E = eU_{\text{bias}}$, which clearly reveals the energy dependence, i.e., the dispersion of the modulation, and very good fits according to Eq. (3). Since the length of the electron scattering wave vector q can therefore be related to the energy E, the 'band' dispersion $E'(q) = E(q) + \epsilon_F$ of the modulation can be determined (see inset of Fig. 3b). This dispersion has a close connection to the band structure of the surface state because q, as mentioned above, is the (elastic) scattering wave vector between two electronic states with opposite momenta $\pm k$, i.e. $q = 2k$. Petersen *et al.* [13] pointed out that a very natural way for determining the scattering wave vector from real-space data such as shown in Fig. 4a is to investigate the data's Fourier transform, shown in Fig. 4b. These data show a ring with a radius that equals twice the Fermi wave vector, i.e. $2k_F$. This reflects that the real-space data have been recorded at

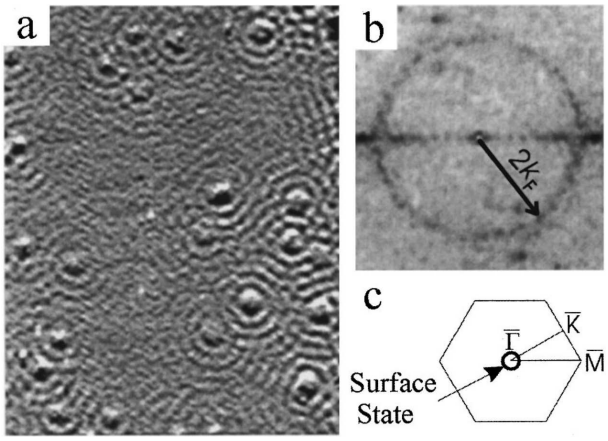

Fig. 4: *(a) Constant current STM image (425×550 Å^2) of Cu(111) obtained at $U_{\rm bias} = -5$ mV, $T = 150$ K, showing a complex pattern of circular waves extending out from point defects. (b) 2D Fourier transform of the image in (a). (c) Sketch of the surface Brillouin zone of Cu(111) with the Fermi contour.*

an energy $E = eU_{\rm bias}$ very close to the Fermi level. Of course, the spatial mapping of Friedel oscillations is in principle viable at other $U_{\rm bias}$. Furthermore, the Fourier analysis allows to extract not only the length but also the direction of the scattering wave vector $\mathbf{q}$, which becomes important when the Fermi surface, or more generally, the electronic constant energy contours (CEC) are not two-dimensional isotropic, in contrast to the case of the Cu(111) surface state. Thus, the investigation of the Friedel oscillations by means of STM/STS, which in connection to superconducting materials has been dubbed *Quasiparticle Interference* (QPI) [14], emerges as a viable route to experimentally obtain fundamental information about the electronic band structure, viz. the band dispersion of electronic states $\xi(\mathbf{k}) = E'(\mathbf{q})$ (with $\mathbf{q} = 2\mathbf{k}$), very much complementary to angular resolved photoemission spectroscopy (ARPES). The advantage of QPI measurements with respect to ARPES is that it allows to access also unoccupied electronic states. Its disadvantage is, however, that $\xi(\mathbf{k}) = E'(\mathbf{q})$ not necessarily holds if the scattering connects different CECs. We shall see examples for this complication further below.

3 Iron-based superconductors

In 2008, superconductivity has been discovered in a compound of the so-called iron pnictide family, viz. the materials $LaFeAsO_{1-x}F_x$ [15]. This has initiated a tremendous research effort which soon yielded a large variety of new superconducting iron pnictide compounds with T_c up to 55 K [16]. All compounds feature Fe_2As_2-layers as the common structural unit, with typical examples being RFeAsO (R=La or Rare Earth), AFe_2As_2 (A=alkaline earth or Eu), LiFeAs and FeSe, which commonly are referred to as '1111', '122', '111' and '11' compounds, respectively (note that Se replaces As in the last example). While the latter two compounds exhibit superconductivity already in their stoichiometric form, the parent materials RFeAsO and AFe_2As_2 are poor metals which exhibit an antiferromagnetic spin density wave (SDW) ground state. Chemical doping destabilizes this state in favor of superconductivity. The obvious proximity of

superconductivity and antiferromagnetism has lead to the conjecture that superconductivity is unconventional in these materials in the sense that spin fluctuations are the driving mechanism of superconductivity with a so-called $s_{\pm}$-wave order parameter [17].
STM/STS has been applied to the iron-based superconductors very rapidly after the discovery of superconductivity. In an initial phase, the experimental work focused on the '122'-, '1111'-, and '11'-phases, where these pioneering studies revealed very valuable information, including topographic investigations of the surfaces, the superconducting gap, vortices, and in few cases even QPI. An essential finding of that period is that for '122' and '1111' reliable STM/STS measurements are complicated by either the presence of surface states, as in '1111' [18, 19], or due to a non-trivial cleaving behavior and surface reconstruction in '122' [20]. A comprehensive review of all these works is given in Ref. [21]. The focus will be instead on one particular material, viz. LiFeAs, for which many of the mentioned difficulties are not an issue, rendering this compound paradigmatic.
Single crystals of LiFeAs exhibit clean, charge neutral cleaved surfaces [22–26] as we shall see below, with a bulk-like electronic structure at the surface [27]. LiFeAs is a *stoichiometric* superconductor, i.e., superconductivity occurs without any doping, at a relatively high critical temperature $T_c \approx 18$ K [28]. This renders it very different from the canonical '1111' and '122' iron-arsenide superconductors where the SDW instability is believed to be related to strong Fermi surface nesting. In the next sections we will discuss how STM/STS can contribute to revealing more details about the compound's electronic structure and the superconducting state.

3.1 Gap spectroscopy

Already long time before the invention of the scanning tunneling microscope [29], the pioneering work of Giaever [30, 31] and Rowell *et al.* [32] on electron tunneling through planar tunneling junctions with one or two superconducting electrodes provided fundamental insights into the nature of superconductivity. This concerns the revelation of both the gap in the quasiparticle tunneling spectrum [30, 31] as well as the signatures of the phonon density in the quasiparticle DOS of a conventional strong-coupling superconductor [32, 33], which have been understood as basic supporting evidence of the theories of Bardeen, Cooper and Schrieffer (BCS) [34] and Eliashberg [35], respectively, showing that the electron-phonon interaction is responsible for the Cooper pairing in conventional superconductors.
We give a brief reminder of some basic considerations of the superconducting state: According to BCS theory, the Bogoliubov quasiparticle bands E_k are connected to the normal state electronic bands ξ_k through $E_k^2 = \xi_k^2 + \Delta_k^2$, where Δ_k generally is a momentum dependent energy gap (see Fig. 5a for illustration). For simplicity, we neglect this momentum dependence, a situation which occurs in purely isotropic s-wave superconductors. If one performs tunneling spectroscopy on such a superconductor in the normal state (here always with a normal-state tip) one finds a linear dependence of the tunneling current I of the bias voltage $U_{\rm bias}$ (see Fig. 5b) if an idealized energy independent DOS as measured by dI/dU (see Fig. 5c) is present. In the superconducting state, however, the gap Δ opens. Hence, the quasiparticle DOS becomes zero

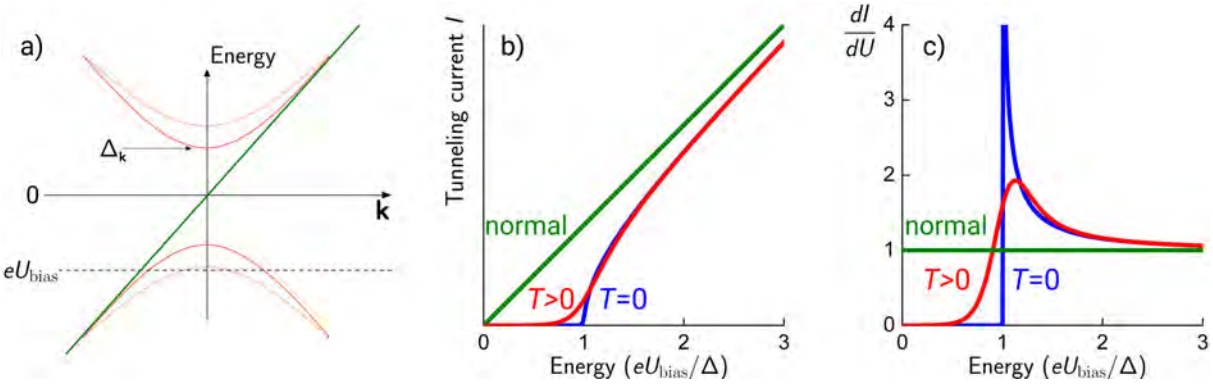

Fig. 5: *(a) Sketch of an electronic band ξ_k (green) and of Bogoliubov quasiparticle bands E_k (red). The dashed curve indicates Bogoliubov states at different momenta for the case of a momentum dependent gap. (b) and (c): Idealized tunneling current I and differential conductance dI/dU for the superconducting state at $T = 0$ (blue) and $T > 0$ (red) and in the normal state (green).*

at $eU_{\rm bias} < \Delta$ and is strongly enhanced at higher energy with a divergence towards $eU_{\rm bias} = \Delta$. In the tunneling experiment, this drastically changes I and dI/dU in the vicinity of Δ: since essentially no current flows up to Δ, it remains largely suppressed with respect to the normal state. Even more interesting is dI/dU, as it directly reflects the quasiparticle DOS, convoluted with the thermal broadening according to Eq. (2) (see Fig. 5c). This means that the differential conductance would reproduce the quasiparticle DOS only a $T \to 0$. In reality, there is of course always some inevitable finite thermal broadening, which enhances dI/dU at energies below the gap and broadens the divergence at Δ into a peak. The latter is usually referred to as *quasiparticle coherence peak*. Note, that the Bogoliubov quasiparticle states are particle-hole symmetric (as is indicated in Fig. 5a), i.e. one expects $dI/dU = -dI/dU$. Thus, the distance between the two coherence peaks in a tunneling spectrum provides convenient means to determine 2Δ.

In unconventional superconductors the situation is typically more complicated than sketched above. The superconducting order parameter could possess nodes as is the case for d-wave superconductors. Since the STS averages over all momenta, this results in a 'V'-shaped dI/dU spectrum as compared to the 'U'-shaped one of s-wave superconductors. This situation is, e.g., realized in cuprate superconductors. In iron-based superconductors, the Fermi surface is characterized by multiple pockets which are expected to possess differently sized and even anisotropic gaps. The tunneling spectrum should provide respective information, ideally by exhibiting multiple coherence peaks. Thus, STS on a superconductor with unknown order parameter structure can already provide crucial information on the order parameter symmetry.

The currently available data on LiFeAs [23, 24, 36] nicely illustrate the capabilities of STS. Fig. 6a shows an overview dI/dU spectrum [23] for $U_{\rm bias} = [-100\ {\rm mV}, 100\ {\rm mV}]$. The data immediately tell, that, apart from the superconducting gap near zero sample bias, the normal state DOS is far from being constant in energy as is assumed in the simplified conditions discussed above. The origin of the strong variation is not yet clarified for this compound. It is however reasonable to understand it as a consequence of the complicated band structure of the

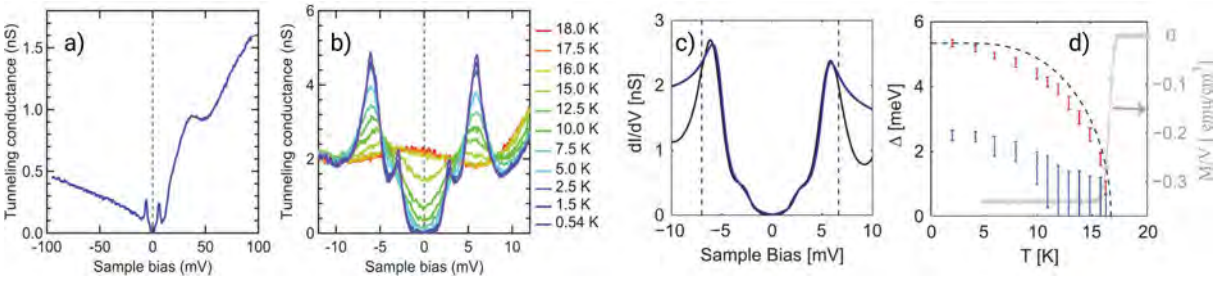

Fig. 6: *(a) Tunneling dI/dU spectrum of LiFeAs at 1.5 K in a large energy window. (b) Low-energy tunneling spectra at different temperatures. Two gaps are visible in the spectra and both gaps disappear above 18 K. Figures (a) and (b) are taken from [23]. (c) Two isotropic gaps fit (blue line) on top of measured dI/dU spectrum (black line, 2 K). The dashed lines indicate the fitting bias range from -6.8 to 6.8 mV. (d) The large gap determined by isotropic s-wave fits (red error bars) generally follows the temperature dependence predicted by the BCS weak coupling limit (dashed black line). The development of the smaller gap (blue error bars) is obscured by thermal broadening at elevated temperatures. The bulk T_c can be inferred from SQUID magnetometry data with a 1 G magnetic field (gray dots and right y axis). Figures (c) and (d) are taken from [24].*

material. Despite the strong apparent asymmetry, the tunneling data in the superconducting state (Fig. 6b) [23] is practically particle-hole symmetric at the lowest investigated temperature, as expected for the density of states of Bogoliubov quasiparticles. Interestingly, the data reveal two peaks on either polarity, one approximately at ± 6 mV, the other at about ± 3 mV. In view of the above considerations, these findings directly imply that at least two different predominant gap sizes are present in this material. Both gaps have no nodes, as revealed by the completely suppressed tunneling conductance dI/dU in a finite energy interval around zero bias voltage. This very clearly excludes d-wave type gaps to be relevant in this compound. STS can not reveal where in momentum space these gaps are located at. Further, complementary information from momentum sensitive techniques such as ARPES is indispensable to elucidate this question.

Before we come back to this point further below, it is interesting to investigate the temperature evolution of the dI/dU spectra. Upon increasing the temperature, the data in Fig. 6b show that the thermal broadening rapidly smears out the detailed gap features as already at $T \gtrsim 5$ K the signatures of the smaller gap have practically vanished. Chi *et al.* [24] nevertheless undertook the attempt to determine the temperature dependence of both gap features through fitting the spectra with an appropriate two-gap formula (Fig. 6c). The result shown in Fig. 6d suggests that the large gap follows a BCS-type temperature dependence with a gap closing at $T_c \approx 17$ K. However, such a statement is not possible for the smaller gap, obviously due to the thermal smearing.

Nag *et al.* have addressed the evolution of the differential conductance in the vicinity of T_c in more detail, by carefully studying spatially averaged dI/dU-spectra within a well-defined area as a function of temperature [36]. Fig. 7a depicts the averaged spectra for all temperatures which reveal an interesting and unexpected temperature evolution of superconductivity. At first glance, the data suggest the onset of superconductivity at $T_c = 16$ K, signalled by a clear depletion of the

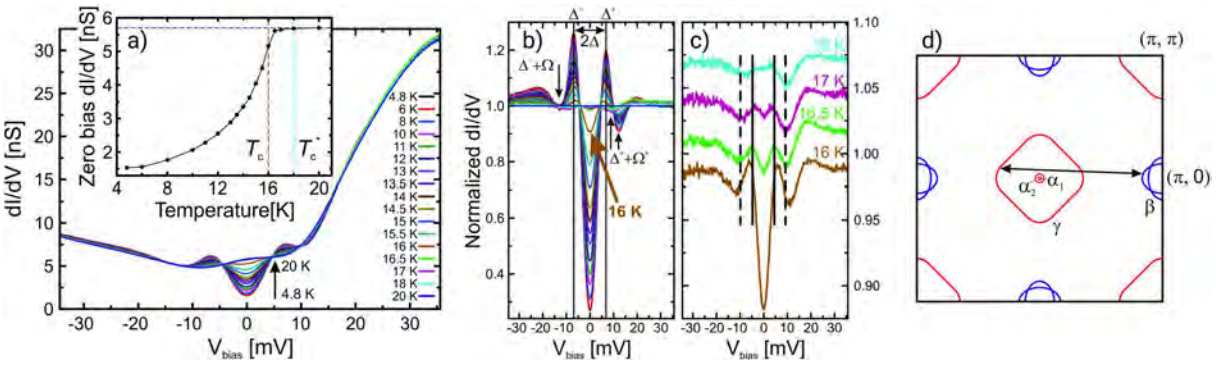

Fig. 7: *a) Temperature dependent tunneling spectra of LiFeAs measured between 6 K and 20 K. The up-arrow indicates the order of the curves at $U_{\rm bias}$ = 0 with increasing temperature. Inset: Zero bias differential conductance as a function of temperature. The horizontal dashed line is a guide to the eye. Vertical dashed lines indicate T_c and T_c^*, see text. b) Waterfall representation of the differential conductance dI/dU for various temperatures. The spectrum at 16 K is highlighted in bold. Black up-arrows indicate the shift of the position of the positive energy dip at $\Delta^+ + \Omega^+$ towards lower energy upon raising the temperature through $T_c = 16$ K. The down-arrow indicates the coarse position of the negative energy dip at $-\Delta^- - \Omega^-$. c) Waterfall representation of normalized spectra in c) at 16 K to 18 K. Superconducting coherence peaks and dip positions at 17 K are indicated by solid and dashed vertical lines, respectively. d) Schematic diagram of the first Brillouin zone (one-Fe unit cell) in LiFeAs based on ARPES data [37]. The indicated γ- and β- pockets possess only a weak k_z-dispersion while the α_1- and α_2-pockets are located only close to $k_z = \pi$. The back arrow indicates the incommensurate spin fluctuation between the γ- and the β-bands observed by Qureshi et al. [38–40]. Figures taken from [36].*

LDOS near zero bias voltage. However, closer inspection of dI/dU at zero bias voltage (inset of Fig. 7a), and in particular after normalizing the data with respect to the normal state (Fig. 7b and c) yields that even at higher temperature clear spectral features of superconductivity are present already at $T \lesssim 18$ K, i.e., a slightly reduced zero-bias dI/dU and particle-hole symmetric coherence peaks at $\Delta^{\pm}$ together with a pronounced dip at $eU_{\rm bias} = \Delta^{\pm} \pm \Omega^{\pm}$ followed by a hump. These features are clearly present at all temperatures $T \lesssim T_c^* = 18$ K, but concern at $T > 16$ K only a tiny portion of the LDOS. Nag *et al.* concluded from this observation that two distinct superconducting phases exist in this material: upon cooling one sets first in at $T_c^* = 18$ K, however being supported only by a very small portion of the Fermi surface, whereas full superconductivity, i.e., supported by all Fermi surface pockets, sets in at $T_c = 16$.

We have seen up to here that STS is capable to provide very comprehensive information about the superconducting gap even for a complicated material like LiFeAs which possesses multiple Fermi surface pockets. However, since STM/STS is (unless QPI is invoked) not momentum resolving, the further interpretation of the data requires the combination with, e.g., ARPES data. For LiFeAs, several high-resolution ARPES studies [41–43] consistently suggest a Fermi surface as sketched in Fig. 7d. It consists of quasi two-dimensional hole-like (labeled γ) and electron-like pockets (labeled β) centered around $\Gamma = (0,0)$ and $M = (\pm\pi, 0)$ or $(0, \pm\pi)$, respectively. Two further hole-like Fermi surface pockets (labeled α_1 and α_2) are centered

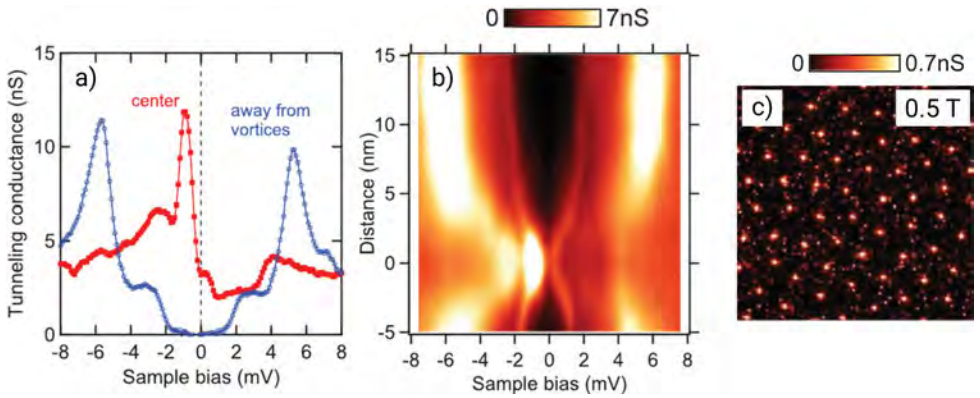

Fig. 8: *a) Tunneling spectra of LiFeAs taken at the center of vortex (red) and away from vortices (blue). b) Line profile of tunneling conductance across the vortex center along the nearest Fe-Fe direction. c) Image of vortices at 1.5 K obtained by mapping the tunneling conductance at* ϵ_F*. The tip was stabilized at* $U_{\rm bias} = +20$ *mV and* $I = 100$ *pA.* $U_{\rm mod} = 0.7$ $mV_{\rm rms}$*. Images taken from [23].*

around the Z-point. Since the latter are tiny, Nag *et al.* [36] concluded these to be natural candidates for supporting the faint superconductivity at $16\ {\rm K} < T < 18$ K. Interestingly, these pockets have been observed in ARPES to possess the largest superconducting gap $\Delta_\alpha \approx 6$ meV as compared to $\Delta_{\gamma,\beta} = 3.5$ to 4 meV at the γ- and β-pockets [42,43]. With this information the larger superconducting gap discussed for Fig. 6 can now be assigned to exactly the α-pockets, whereas the smaller gap is connected to either the γ- or the β-pockets, or both.

There is even more information provided by the dI/dU-spectra, viz. through the dip-hump structures at $eU_{\rm bias} = \Delta^{\pm} \pm \Omega^{\pm}$ in Fig. 7, the signatures of which are already apparent in the unnormalized spectra shown in Fig. 6b and c. These details have been much debated in terms of a bosonic mode of energy Ω that couples to the electrons and which should give rise to clear anomalies in the quasiparticle DOS [35,33]. Chi *et al.* suggested [24] an antiferromagnetic spin resonance as the nature of the bosonic mode. In contrast, Nag *et al.* pointed out [36] that this is not supported by the temperature independence of Ω, which in case of the dip being connected to an antiferromagnetic resonance should track the temperature dependence of order parameter, and the de facto absence of an antiferromagnetic resonance in inelastic neutron scattering results on LiFeAs [38,39]. It is interesting to note that recent theoretical work [44] suggested inelastic tunneling processes to play a very important role in the interpretation of the dip-hump feature.

3.1.1 Vortex spectroscopy

In the above considerations, the spatial dependence of the superconducting state did not play a role, i.e., the particular strength of STM/STS to spatially resolve electronic structure has not been exploited. This is in order as long as the material exhibits a spatially homogeneous superconducting state, which is often the case. A very obvious situation where the superconducting state is spatially inhomogeneous is the Shubnikov phase of a type-II superconductor, where magnetic flux lines (vortices) enter the superconducting volume. Each flux line holds one mag-

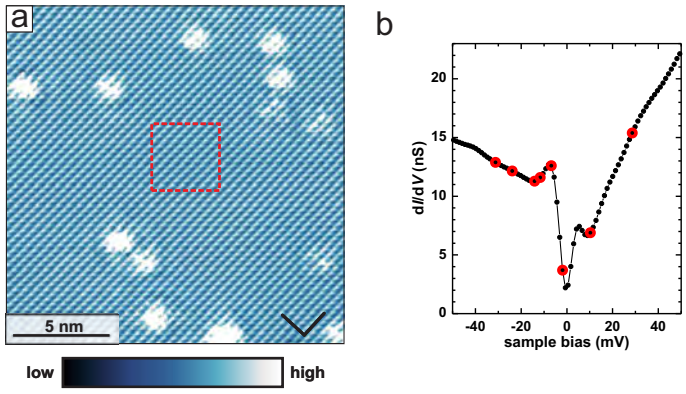

Fig. 9: *(a) Surface topography of LiFeAs measured in constant current mode ($I = 600$ pA, $V_{\mathrm{bias}} = -50$ mV) taken at $T \approx 5.8$ K. Black arrows indicate the direction of the lattice constants [28] with $a = 3.7914$ Å. (b) Spatially averaged tunneling spectrum taken in the square area (dashed lines) in (a). The spectrum exhibits a gap with $2\Delta \sim 10$ mV, which (taking thermal broadening into account) is consistent with low-temperature (~ 500 mK) tunneling data in Fig. 6 of the superconducting gap of LiFeAs. Representative energy values for further QPI analysis in Fig. 10 are marked by red circles. Figure taken from [22].*

netic flux quantum $\phi_0 = h/(2e)$. The magnetic field is maximum inside the vortex core and then radially decays on a length scale given by the London penetration depth λ_L. At the same time, the superconducting wave function decays from outside towards zero at the vortex core with the Ginzburg-Landau coherence length ξ_{GL} as the determining length scale. This has a strong impact on the LDOS measured at the vortex core, because it should be enhanced at energy values inside the superconducting gap with respect to the superconducting LDOS. This is indeed the case also for LiFeAs as is shown in Figure 8. Hanaguri *et al.* [23] report a complete suppression of the both sets of coherence peaks in favor of pronounced and asymmetric vortex core states inside the gap (Fig. 8a). Fig. 8b shows the spatial evolution of the spectrum along the Fe-Fe direction. In principle, one can expect interesting information about the nature of the superconducting order parameter from such spatial studies. However, it has been pointed out by Wang *et al.* [45] that it is *a priori* difficult to disentangle the effect of order parameter symmetry from anisotropy effects of the Fermi surface.

The enhanced LDOS at the vortex core leads to an enhanced value of the differential conductance dI/dU and thus can be used to visualize the structure of the vortex lattice as is exemplified in Fig. 8c. The investigation of such vortex matter is a separate field as such. The interested reader is referred to the original literature [23, 45] and references therein.

3.2 Quasiparticle interference

In the following we begin by largely following the first experimental paper on the QPI of LiFeAs [22]. Afterwards, we compare and discuss the earlier findings with more recent publications [26, 46, 47]. Prior to performing QPI measurements it is important to have a good account on the surface to be investigated which can be achieved by topographic STM mea-

surements. Fig. 9a shows a representative topography of the presumably Li-terminated surface taken at low-temperature (~ 5.8 K) after cleaving a crystal [22]. The data reveals a highly periodic atomically resolved surface layer and several impurity sites. A spatially averaged dI/dU spectrum, taken on a defect-free area clearly reveals a superconducting gap (Fig. 9b). Subsequently, a full-spectroscopic map was recorded on this surface as described before in section 2.1.2: STS was measured at each of the 256×256 pixel by stabilizing the tip with feedback loop engaged at a setpoint of $U_{\mathrm{bias}} = -50$ mV and $I = 600$ pA followed by subsequently ramping U_{bias} to $+50$ mV with the feedback loop switched off. During ramping the voltage $I(U_{\mathrm{bias}})$ and $dI/dU(U_{\mathrm{bias}})$ were recorded where a lock-in amplifier with a modulation voltage $U_{\mathrm{mod}} = 1.2$ mV (RMS) and a modulation frequency $f_{\mathrm{mod}} = 3.333$ kHz was used.

dI/dU maps at representative energies (Fig. 10a-h) show very clear QPI patterns which are most pronounced at energies in the vicinity of the coherence peaks at negative energy ($U_{\mathrm{bias}} \gtrsim -20$ mV). In this energy range, the QPI is clearly not only visible in real space as relatively strong modulations close to the defects but also appears as clear wave-like modulations (with a wavelength of a few lattice spacings) in the relatively large defect-free area in the center of the field of view. QPI patterns are also discernible at positive energy, but compared to the pronounced modulations at negative values, the amplitude of the modulations decay more rapidly when moving away from a defect.

In analogy to the previous example on the Cu(111) surface the real space data were Fourier-transformed in order to extract the wave vectors of the QPI at each of the measured energies. Figures 10i-p reveal a very rich structure which we discuss now in detail: The least interesting features of the data show at all energies bright spots at $(\pm\pi, \pm\pi)$ and at higher $\mathbf{q}$ (the choice of reciprocal coordinates refers to a one-iron unit cell). These result from the atomic corrugation in the real space images. The most salient feature is, however, a bright structure distributed around $\mathbf{q} = (0, 0)$. In similarity to the observed real-space modulations this feature is particularly pronounced at energies $U_{\mathrm{bias}} \approx [-20\ \mathrm{mV}, 0]$ where it attains a squarish shape with the corners pointing along the $(q_x, 0)$ and $(0, q_y)$ directions. Upon increasing U_{bias} to positive values, the intensity at the square corners increasingly fades and for $U_{\mathrm{bias}} > 10$ mV the squarish shape changes to an almost round structure which remains in that shape up to 50 mV. The Fourier transformed images also reveal further well resolved structures with significantly lower intensity centered around $(\pi/2, \pi/2)$, $(\pi, 0)$ and (π, π) which again are most pronounced between -20 mV and the Fermi level. At more negative bias, these finer structures fade, while at positive bias voltage they develop into a rather featureless diffuse background.

These rather complicated Fourier-transformed images directly account for the relevant scattering wave vectors in the QPI, and thus allow to deduce important qualitative information about the electronic structure of LiFeAs. However, one should stay extremely cautious when seeking the extraction of quasiparticle bands from the scattering image, as this is not straightforward, in contrast to one-band systems, such as the Cu(111) surface state. In order to illustrate this difficulty, we will now first show how the observed scattering vectors can clearly be assigned to particular scattering processes if other experimental data for the electronic band structure deduced from ARPES experiments [41] are taken into account. Afterwards, we will point out

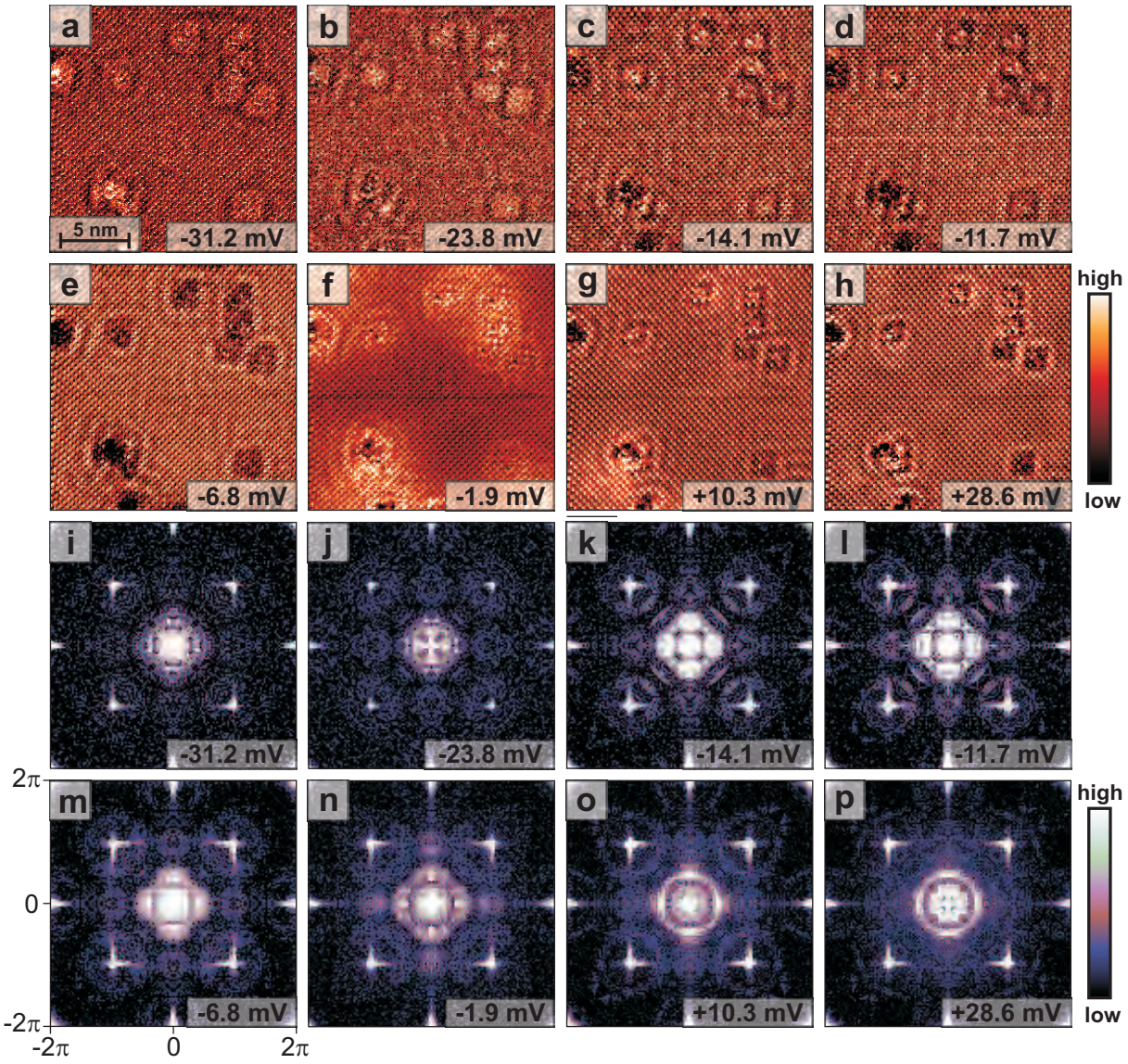

Fig. 10: *(a-h) SI-STM maps of the region shown in Fig. 9 at selected representative bias voltages. (i-p) Fourier transformed images of the maps shown in a-h. Bright spots at* $(\pm\pi, \pm\pi)$ *and at higher* $\mathbf{q}$ *result from the atomic corrugation in the real space images. Figure taken from [22].*

an alternative interpretation of the data [26], which, however, is not compatible with the compound's electronic structure.

Fig. 11a and b compare the CEC of LiFeAs at $E = -11.7$ mV derived from ARPES data [41] with the observed QPI intensities in the Fourier transformed image. Most prominent is that the observed central squarish structure in Figure 11b appears like a somewhat enlarged smeared replica of the large, hole-like CEC of the γ-band around $(0, 0)$. This observation can directly be understood as stemming from interband scattering processes ($\mathbf{q}_1$) connecting the very small CEC of the α-bands[2] and the larger squarish-shaped γ-CEC around $(0, 0)$. Furthermore, the much weaker structure at $\mathbf{q} = (\pi, 0)$ in Fig. 11b apparently can be rationalized as stemming

[2]For simplicity we do not distinguish between the α_1 and α_2-bands.

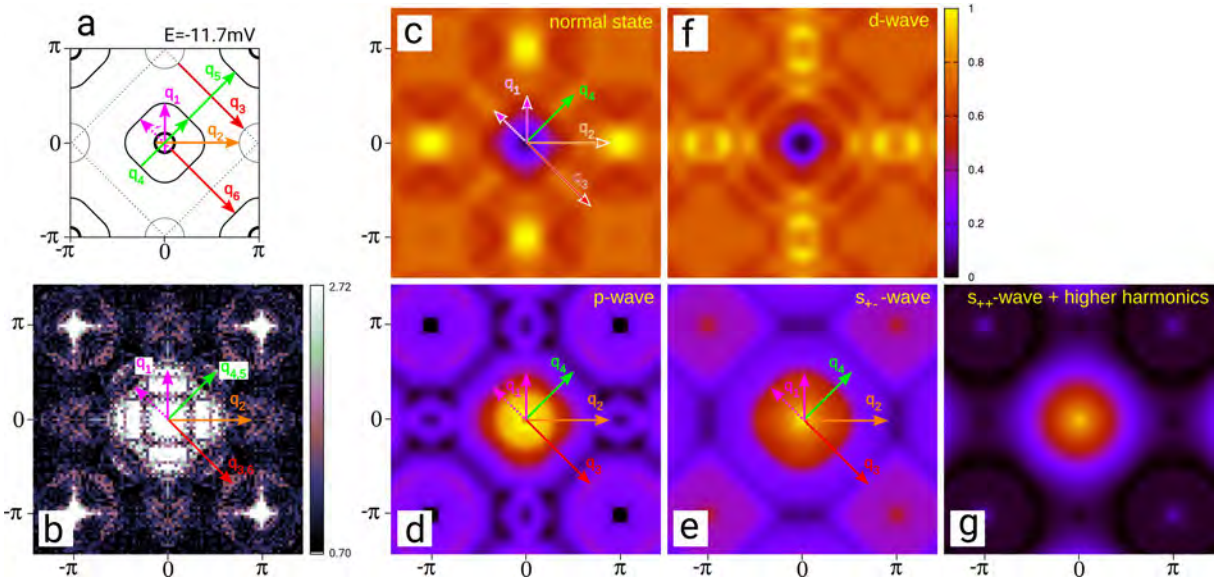

Fig. 11: *(a) Simplified CEC [41] at $E = -11.7$ meV in the periodic-zone scheme of the Brillouin Zone (BZ), where the first BZ (referring to the unit cell with two Fe atoms) is indicated by the dashed lines. However, the used coordinates in reciprocal space refer to the unit cell with one Fe atom, in order stay consistent with the theoretical work in Ref. [48]. This choice of reciprocal coordinates leads to Bragg-intensity at $(\pm\pi, \pm\pi)$ instead of $(\pm 2\pi, 0)$ (and $(0, \pm 2\pi)$) as one would expect for a two-Fe unit cell. The two pockets around $(0, 0)$ represent hole-like CEC while the pockets at the zone boundary are electron-like. $\mathbf{q}_{1,2}$ represent scattering processes which connect states on the small hole-like CEC and on other CEC, $\mathbf{q}_3$ and $\mathbf{q}_4$ represent scattering between the electron-like and within the large hole-like CEC, respectively. $\mathbf{q}_{5,6}$ represent umklapp processes. Note that each scattering process $\mathbf{q}_{1,\ldots,6}$ is described by a set of scattering vectors as is illustrated for $\mathbf{q}_1$ (dashed and solid arrows). (b) Measured Fourier transformed image at the same energy (the same as in Fig. 10l) with $\mathbf{q}_{1,\ldots,6}$ superimposed. The most salient QPI features around $(0, 0)$ and $(\pi, 0)$ match well with $\mathbf{q}_1$ and $\mathbf{q}_2$ (see text). The further observed but less prominent QPI intensities around (π, π) and at $(\pi/2, \pi/2)$ are well described by $\mathbf{q}_3$ and $\mathbf{q}_4$, respectively. The umklapp scattering vectors $\mathbf{q}_5$ and $\mathbf{q}_6$ might also be of relevance here. (c-g) Calculated QPI in $\mathbf{q}$ space assuming the normal state and a superconducting order parameter with $s_{\pm}$-, d-, p-, and s_{++} symmetry. Figure taken from [22].*

from interband scattering processes ($\mathbf{q}_2$) connecting the electron-like CEC of the β-bands with again the small α-CEC. The further observed but less prominent QPI intensities around (π, π) and at $(\pi/2, \pi/2)$ are well described by $\mathbf{q}_3$ and $\mathbf{q}_4$, respectively, which represent scattering between the electron-like β-CEC and within the large hole-like γ-CEC, respectively. $\mathbf{q}_{5,6}$ represent umklapp processes, which might also be of relevance here.

An analogous analysis can be performed at other energies. Fig. 12a and b show QPI data and a corresponding assignment to scattering processes for $E = -6.8$ meV [46], where the focus is just on small scattering vectors. Here, the contour of $\mathbf{q}_1$ in the QPI image is particularly sharp. The comparison between the QPI scattering image and the band structure can of course be undertaken on a much deeper level through comparing the experimental QPI image with calculations of the QPI pattern based on the electronic band structure of the compound. For

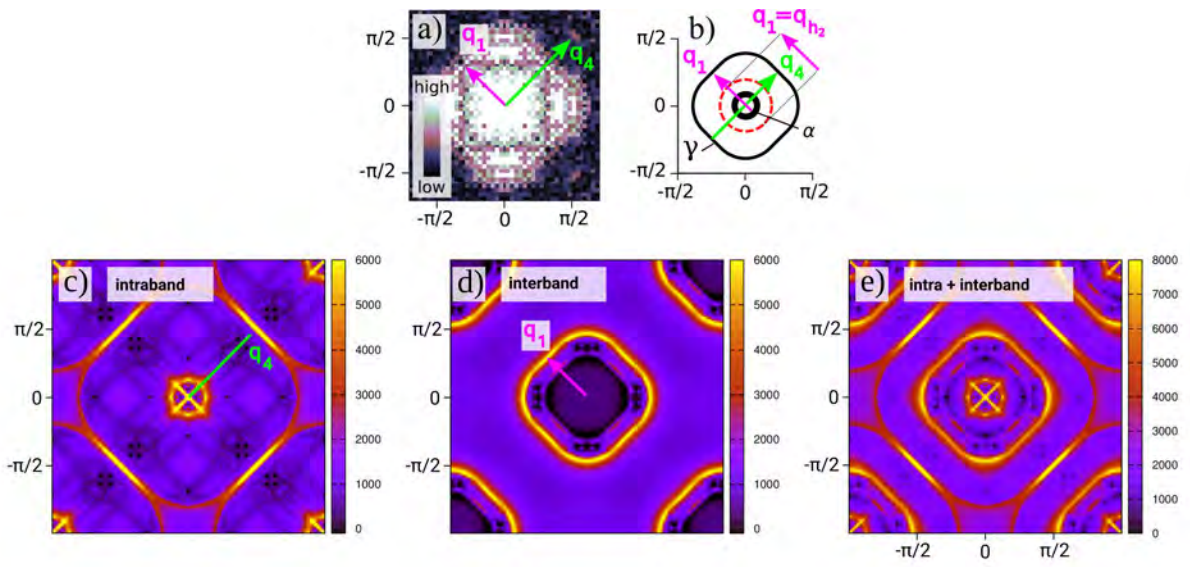

Fig. 12: *(a) Fourier transformed QPI data of LiFeAs at $E = -6.8$ meV ((the same as in Fig. 10m). (b) Simplified constant energy contours (CEC) of the hole-like α and γ bands at $E = -6.8$ meV. $\mathbf{q}_1$ represents interband scattering processes which connect states on both bands. It has the same length as $\mathbf{q}_{h_2}$ (i.e., the diameter of the dashed h_2-CEC) reported in Ref. [26]. $\mathbf{q}_4$ represents intraband scattering within the γ band. (c-e) Numerical simulation of the QPI patterns applied to a tight-binding model of the ARPES results [41, 43]. (c) Only intraband scattering within the small, hole-like band α and the large, hole-like band γ is considered. All scattering processes between α and γ and those processes involving the electron bands are suppressed in the calculation. (d) Only interband scattering between α and γ is considered. (e) Contributions displayed in panels (c) and (d) are summed up in order to enable the comparison of the intensities. The scattering vectors $\mathbf{q}_1$, $\mathbf{q}_4$ (see a, b) are indicated. Figures taken from [46].*

LiFeAs, high-precision band structure data exist. The corresponding theoretical results for the QPI are depicted in Fig. 12c to e, where intraband scattering processes within the γ-CEC (c) and interband scattering processes between the α-CEC and the γ-CEC (d) have been considered separately. Only when summed up (e), these account for the experimentally determined scattering image.

A different conclusion concerning the compatibility with ARPES is, however, reached by another QPI study on LiFeAs [26], despite geometrically very similar QPI data of excellent quality. The authors of this work attempted the very difficult task to reconstruct the band structure of LiFeAs solely based on QPI data. In order to circumvent the problem that QPI provides only access to elastic scattering vectors, i.e., the relative momentum difference of two different states at a given energy, they suggested that the QPI emerges solely from *intraband* scattering within the separate hole-like bands. Based on this assumption, the extracted scattering vectors have been used to construct three hole-band dispersions along high-symmetry directions. One of the resulting bands (labeled h_3 in Ref. [26]) is in good agreement with the size of the larger hole-like Fermi surface observed in ARPES [41,43,42], and another (h_1) matches quite well the α-bands. However, the third of the suggested bands (h_2) lacks such a correspondence since its

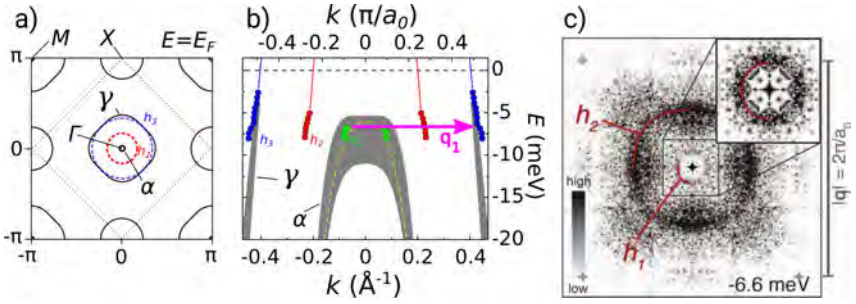

Fig. 13: *a) Schematic illustration of the Fermi surface (FS) sheets of LiFeAs. Solid lines illustrate the approximate size of the FS sheets as observed by ARPES [41, 49, 42, 43], dashed lines correspond to the hole-like FS resulting from the hole-like bands h_2 and h_3 as obtained from QPI by Allan et al. [26]. Note that Allan et al. extract the Fermi wave vectors along high-symmetry directions and that the shown FS sheets are respective isotropic two-dimensional extrapolations. The shown unfolded Brillouin zone (BZ) refers to the one-Fe unit cell. The BZ related to the two-Fe unit cell is indicated by dotted lines. b) LiFeAs band structure at negative energies. Circles represent the extracted quasiparticle dispersions E_k of the hole-like bands h_1, h_2, h_3 obtained in [26], where k is given by half of the length of the observed scattering vectors* $\mathbf{q}$*. Grey shaded contours represent α and γ bands as observed by ARPES [41, 49, 42, 43]. The extended width of the α band indicates k_z dependence obtained from different photon energies [43]. The indicated dispersion shown as a dashed line corresponds to data obtained at a photon energy $h\nu = 20$ eV. Figure taken from [46]. c) Fourier transformed QPI data of LiFeAs at $E = -6.6$ meV, taken from [26]. Note that the data refer to the two-Fe unit cell, in contrast to the data in Figures 10, 11, and 12 which causes a rotation of the coordinate system by 45°.*

Fermi wave vector $k_F \approx 0.2$ Å^{-1} [26] neither matches that of the large γ nor the small hole-like α Fermi surfaces observed in ARPES, see Fig. 13a.

Fig. 13b depicts the dispersion of all three bands h_1, h_2, and h_3. In fact, the QPI structure which has been used to extract the h_2 is geometrically very similar to the $\mathbf{q}_1$-contour in Figures 10 and 12, see the corresponding data in Figures 12 and 13. This means that the QPI intensity in Fig. 13, which has been interpreted to stem from *intraband* scattering of a hypothetical h_2 band which is unsupported by other methods like ARPES or de-Haas-van-Alphen measurements [50], can be well reinterpreted as *interband* scattering as described by $\mathbf{q}_1$ [46].

The latter example illustrates that QPI measurements can provide very valuable insights into a compound's electronic structure, in particular the electronic band structure. The caveat is, however, that QPI is not capable to provide direct information about quasiparticle states because it is only sensitive to the scattering states. Thus, one is advised to always complement QPI data with results from other techniques: ARPES and also de-Haas-van Alphen data are well suited for double checking the QPI results. On the other hand, the sensitivity to scattering events potentially brings about access to qualitatively new information which remains inaccessible by other means. We shall introduce some ideas in this respect in the following section.

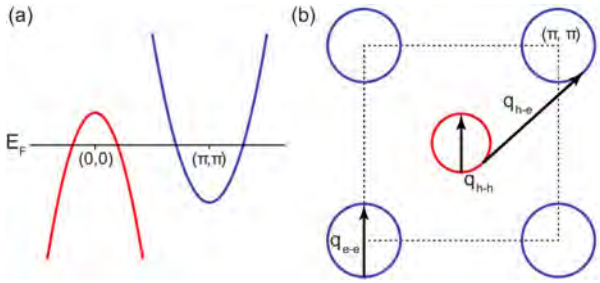

Scenario	$\mathbf{q}$ Suppressed Intensity	$\mathbf{q}$ Enhanced Intensity
nonmag. imp., s_{++}	$\mathbf{q}_{h-h}$, $\mathbf{q}_{e-e}$, $\mathbf{q}_{h-e}$	-
mag. imp., s_{++}	-	$\mathbf{q}_{h-h}$, $\mathbf{q}_{e-e}$, $\mathbf{q}_{h-e}$
nonmag. imp., $s_{\pm}$	$\mathbf{q}_{h-h}$, $\mathbf{q}_{e-e}$	$\mathbf{q}_{h-e}$
mag. imp., $s_{\pm}$	$\mathbf{q}_{h-e}$	$\mathbf{q}_{h-h}$, $\mathbf{q}_{e-e}$

Fig. 14: *(a) A simplified two-band model for the pnictides with a hole-like band centered at* $\mathbf{k} = (0,0)$ *and an electron-like band centered at* $\mathbf{k} = (\pi/a, \pi/a)$*. (b) The Fermi surfaces of the bands in (a). The vectors* $\mathbf{q}_{h\text{-}h}$ *and* $\mathbf{q}_{e\text{-}e}$ *show intraband scattering within the hole and electron pockets, respectively, while* $\mathbf{q}_{h\text{-}e}$ *shows interband scattering between the two. In the* $s_{\pm}$ *scenario* $\Delta_{\mathbf{k}}$ *switches sign between the initial and final states of the* $\mathbf{q}_{h\text{-}e}$ *scattering process, while it remains the same in the* s_{++} *scenario. Image taken from [47]. (c) A summary of the QPI selection rules expected for a pnictide superconductor with* s_{++} *or* $s_{\pm}$*. The QPI intensity of a scattering vector is either suppressed or enhanced inside the superconducting gap relative to the intensity outside the gap. The intensity variations stem from the energy dependence of the coherence factors. The four combinations of two pairing symmetries and two kinds of impurities result in four distinct sets of selection rules. Table taken from [47].*

3.2.1 Accessing the structure of the superconducting order parameter

In the superconducting state the DOS is redistributed by the opening of the superconducting gap. More specifically, in the superconducting state the DOS at energy-values close to the gap value is further boosted in comparison to the normal state since the quasiparticle dispersion $E_{\mathbf{k}} = \pm(\xi_{\mathbf{k}}^2 + |\Delta_{\mathbf{k}}|^2)^{1/2}$ is rather flat (see Fig. 5a). Furthermore, depending on the gap function $\Delta_{\mathbf{k}}$, particular scattering channels are suppressed while others are enhanced according to the coherence factors of the superconducting state. Consequently, the QPI measured at energies $|E|$ close to the averaged gap value will be redistributed, thereby containing detailed information about the structure of the superconducting order parameter. More specifically, the scattering rate between quasiparticle states with momenta $\mathbf{k}$ and $\mathbf{k}'$ is proportional to coherence factors $(u_{\mathbf{k}} u^*_{\mathbf{k}'} \mp v_{\mathbf{k}} v^*_{\mathbf{k}'})$, where the $\mp$ sign is determined by the magnetic/non-magnetic nature of the underlying scattering mechanism. The coherence factors are sensitive to the phase of the superconducting order parameter via the Bogoliubov coefficients $u_{\mathbf{k}}$ and $v_{\mathbf{k}}$ which fulfil the relation $v_{\mathbf{k}}/u_{\mathbf{k}} = (E_{\mathbf{k}} - \xi_{\mathbf{k}})/\Delta^*_{\mathbf{k}}$ with the quasiparticle energy $E_{\mathbf{k}} = \pm(\xi_{\mathbf{k}}^2 + |\Delta_{\mathbf{k}}|^2)^{1/2}$ [34, 51]. Thus, through the coherence factors, the QPI pattern is in principle decisively influenced by the nature of superconductivity, in particular the symmetry of the superconducting gap. Pioneering studies which involve the analysis of QPI data along these lines have been performed on cuprate high-temperature superconductors [52] and, more recently, also for iron-based superconductors [53]. Here, we summarize briefly the currently available results for LiFeAs.

In order to exploit the phase sensitivity of the QPI, Hänke *et al.* [22] calculated the QPI in the superconducting state using an appropriate BCS model for LiFeAs which can describe three cases of elementary singlet pairing (s_{++}, $s_{\pm}$, and d-wave) as well as a p-wave triplet pairing scenario. These calculations were based on a band structure model matching the ARPES results [41] (see

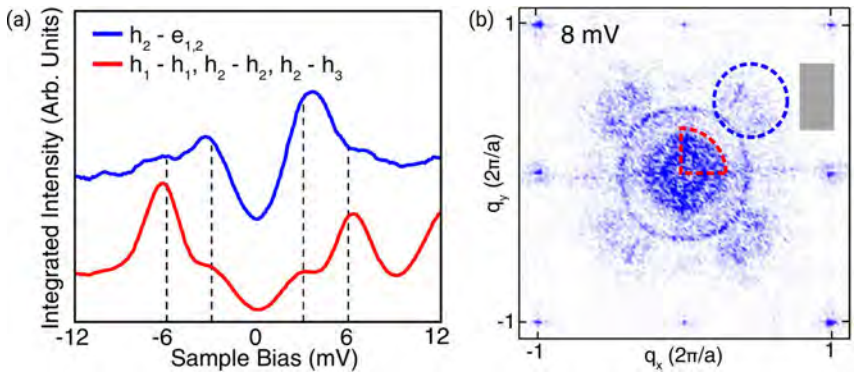

Fig. 15: *(a) The integrated intensity of the QPI signal for the intraband h-h (red) and interband h-e (blue) scattering vectors. The curves are normalized to the value at 12 meV and the interband intensity has been offset for clarity. The dashed lines indicate the values of the superconducting gaps. (b) The red sector and blue circle are the integration windows for intraband h-h and interband h-e scattering intensities in (a), respectively. A noise background signal is integrated in the grey rectangular area and subtracted. Here the windows are shown in one quarter for simplicity but the integration is performed over the equivalent areas in all four quadrants of the image. Image taken from [47].*

Fig. 11c-g for results at $E = -11.7$ mV).[3] One firm qualitative outcome of these calculations was, from the location of the high intensity region around $(0, 0)$, that in the superconducting state the dominating scattering processes are those which connect states on the hole-like bands as it was afore inferred from the mere geometrical analysis shown in Fig. 11(a), (b). The closer examination of the individual QPI patterns revealed a very strong dependence of the pattern on the assumed pairing symmetry. Interestingly, a direct comparison with the experimental result yielded a striking agreement between the experimentally observed QPI and the calculated image of Fig. 11(f), which is the result for a triplet paired state. The agreement is obviously much less pronounced for $s_{\pm}$, s_{++}, and d-wave singlet pairing cases. These qualitative statements also hold at other energies (see [22] for details).

Chi *et al.* come to a different result based on their data [47]. Based on the coherence factor analysis, they derive a set of selection rules which describe the expected enhancement and the suppression of particular scattering vectors upon tuning the energy from values outside to inside the superconducting gap depending on the type of scattering impurity and on the symmetry of the superconducting order parameter, see Fig. 14.

For the analysis, Chi *et al.* introduced to integrate with the scattering data the QPI intensity which belongs to a specific scattering process, i.e., either to intraband scattering h-h within the hole-like CEC or to interband scattering between hole and electron-like CEC h-e. From the very different energy dependence of the integrated QPI intensity for the two regions and the selection rules they conclude a support of a $s_{\pm}$-wave order parameter, see Fig. 15 and [47] for details.

[3] The experimentally observed strong intensity at $\mathbf{q} \sim (0, 0)$ reflects a constant background in the SI-STM maps which is not taken into account in the calculations. Thus there is no enhanced intensity in the calculated Fourier transformed images at $(0, 0)$.

It is worth pointing out that these unsatisfactory conflicting results [22, 47] provide the motivation for ongoing research. Hirschfeld *et al.* have theoretically addressed this problem [54] and suggested to use the temperature dependence of momentum-integrated QPI data in order to give a firm statement on the superconducting gap structure. Experimentally, this is, however, still open.

4 Cuprate superconductors

There exists vast literature which provides excellent introduction to the physics of the cuprate superconductors, see e.g. [55]. What we need to know here is that the electronic phase diagram of hole-doped cuprates has much resemblance to that of the canonical 122 or 1111 iron-based superconductors. One important difference is that the undoped parent state is an antiferromagnetic (charge transfer) insulator. Charge-doping causes its destruction and the emergence of superconductivity with the highest critical temperature T_c known so far (up to $\sim$ 135 K) for ambient pressure conditions [55]. The hole-like Fermi surface consists only of one band (which renders the situation in QPI investigations much simpler as compared to the iron-based superconductors), with a d-wave order parameter in the superconducting state with nodes on the Fermi surface along the $(\pm\pi, \pm\pi)$ directions.

4.1 Quasiparticle interference and the octet-model

In fact, the modern investigation of QPI analysis has first been introduced in pioneering work on the cuprate superconductors [14, 56, 57]. Fig. 16 shows representative experimental data for the material $Bi_2Sr_2CaCu_2O_{8+\delta}$ [56]. The topographic data in Fig. 16a reveal the characteristic BiO-terminated surface of $Bi_2Sr_2CaCu_2O_{8+\delta}$ which exhibits a stripe-like periodic superstructure. Full dI/dU spectroscopic mapping of the same field of view reveals pronounced QPI signatures; representative real space and Fourier transformed data are shown in Figures 16b and (c-f), respectively. The latter reveal multiple high-intensity spots which possess a clear energy dispersion. It has been proposed by McElroy *et al.* [56] that these spots result from quasiparticle scattering between eight specific points in momentum space which emerge in the superconducting state. The situation is illustrated in Fig. 16g which shows 'banana'-shaped quasiparticle CEC which emerge at energies smaller than the maximum $|\Delta_{\mathbf{k}}|$ in the superconducting d-wave state. McElroy *et al.* argued [56] that since the quasiparticle DOS ρ_s at a given energy $E_{\mathbf{k}} = \omega$ is proportional to

$$\int_{E_{\mathbf{k}}=\omega} |\nabla_k E_{\mathbf{k}}|^{-1} \, dk, \tag{5}$$

the primary contributions to $\rho_s(\omega)$ stem from the two tips of the 'banana' where $|\nabla_k E_{\mathbf{k}}|^{-1}$ is largest, and thus the QPI should be dominated by the seven scattering vectors $\mathbf{q}_{1...7}$ which connect the eight 'banana' tips (see Fig. 16g and h). This model has proven to describe the

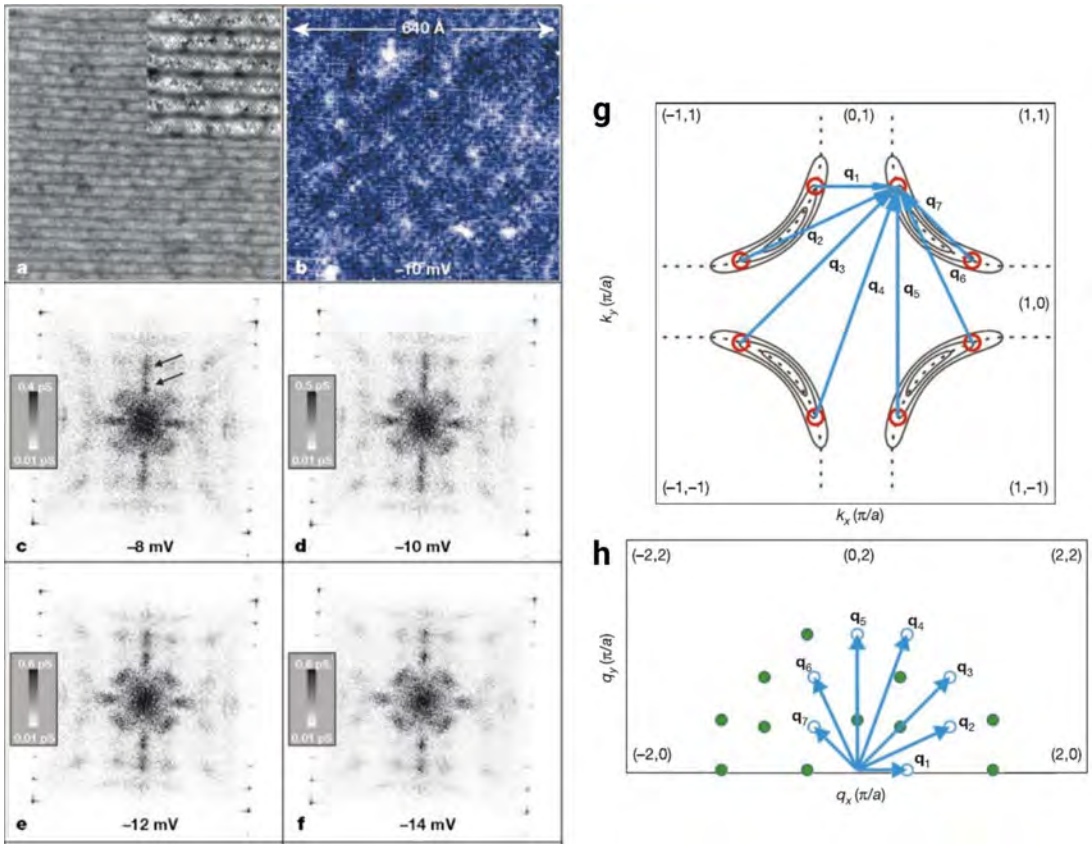

Fig. 16: *Atomic resolution images of the LDOS of $Bi_2Sr_2CaCu_2O_{8+\delta}$ and the resulting Fourier-space images of the wave vectors making up the LDOS modulations. (a) A topographic image of the BiO surface used, with location and resolution identical to the LDOS maps. The $\times 2$ magnification inset (from part of the same image) demonstrates the atomic resolution achieved. (b) Representative example of the real space $g(\mathbf{r}, E) = dI/dU|_{E=eU_{\rm bias}}$ in this field of view. All $g(\mathbf{r}, E)$ were acquired using the same atomic resolution and register. (c-f) Examples of the Fourier transformed $g(\mathbf{q}, E)$. The only non-dispersive signals (which are due to the supermodulation) are marked by arrows in (c). The reciprocal atomic lattice is located at the square of intense points near the corners of each panel. One can readily see 12 of the 16 LDOS modulations of the quasiparticle interference model. The dispersion and evolution of all the wave vectors of these modulations is evident in the differences between frames. (g, h) The expected wave vectors of quasiparticle interference patterns in a cuprate superconductor with d-wave order parameter. (g) Solid lines indicate the $\mathbf{k}$-space locations of several banana-shaped quasiparticle CEC as they increase in size with increasing energy. As an example, at a specific energy, the octet of regions of high $|\nabla_{\mathbf{k}} E_{\mathbf{k}}|^{-1}$ are shown as red circles. The seven primary scattering $\mathbf{q}$-vectors interconnecting elements of the octet are shown in blue. (h) Each individual scattering $\mathbf{q}$-vector from this set of seven is shown as a blue arrow originating from the origin in $\mathbf{q}$-space, and ending at a point given by a blue circle. The end points of all other inequivalent $\mathbf{q}$-vectors of the octet model (as determined by mirroring each of the original seven in the symmetry planes of the Brillouin zone) are shown as solid green circles. Thus, if the quasiparticle interference model is correct, there would be sixteen inequivalent local maxima in the inequivalent half of $\mathbf{q}$-space detectable by Fourier transformed STS. Images taken from [56].*

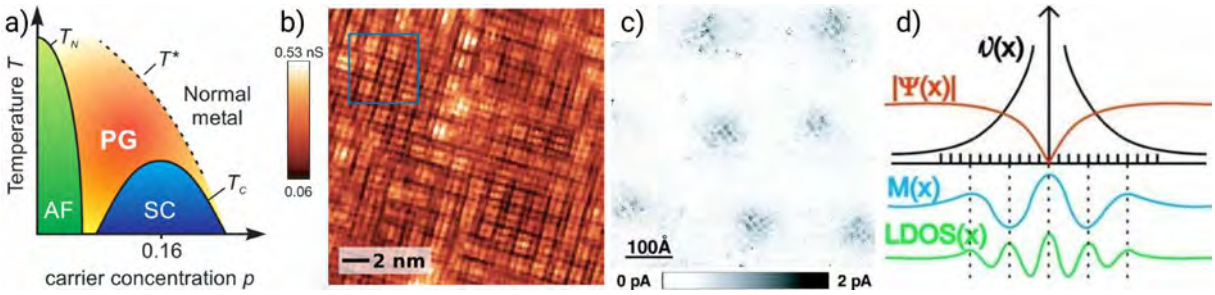

Fig. 17: *a) Schematic electronic phase diagram of the cuprates showing the antiferromagnetic parent phase (AF), the superconducting phase (SC) and the pseudogap-phase (PG). Image taken from [58]. b) Spectroscopic map of $Ca_{1.9}Na_{0.1}CuO_2Cl_2$ at $E = 24$ meV in the superconducting state. Image taken from [59]. c) Magnetic-field induced additional LDOS at magnetic vortex cores of $Bi_2Sr_2CaCu_2O_{8+\delta}$. d) A schematic model of the electronic/magnetic structure of the vortex core showing the superfluid velocity v, the superconducting order parameter $|\Psi|$, LDOS, and the anticipated periodicity of the spin density modulation M. Images taken from [60].*

QPI in a compelling way and referring to the eight momentum space points has been dubbed 'octet-model'.
Hanaguri *et al.* [52] extended the octet model by adding, for the first time, a coherence factor analysis which has been ground-breaking for all later experimental and theoretical work in this direction.

4.2 Nanoscale electronic order

In the cuprates, the emergence of superconductivity from the antiferromagnetic parent state is accompanied by the so-called pseudogap phase (see Fig. 17a). Evidence is growing that electronic order within the pseudogap phase is a crucial bit for understanding the electronic phase diagram of the cuprates and eventually the nature of superconductivity in these compounds [61, 62]. The correlation lengths of the electronic order often are relatively short which renders it challenging to be detected by neutron or X-ray diffraction techniques. Spectroscopic imaging STM, as local probe, therefore played an important role to reveal the electronic ordering states in the cuprates. In the experiments the electronic order manifests as CDW-like electronic superstructures, see, e.g., data by Hanaguri *et al.* [59] in Fig. 17b. These states seem to compete with superconductivity, as their amplitude is enhanced when superconductivity is suppressed, e.g., in the core of a magnetic vortex [60] (see Fig. 17c and d.)

5 Conclusion

In this lecture we have seen which possibilities a low-temperature scanning tunneling microscope offers to investigate the physics of correlated electron systems. This included an introduction to the most important measurement modes for microscopy and spectroscopy and the concept of studying the quasiparticle interference for achieving even momentum space information from real space data. The system which we focused on, LiFeAs, offers the advantage

that clean experimental data exist that allow to discuss many different aspects of scanning tunneling spectroscopy and the different types of information that can be gained. Further aspects of scanning tunneling spectroscopy of correlated materials were introduced through briefly discussing important work on cuprate superconductors. Thus, this lecture, together with the given literature, should provide the necessary basis for understanding the work on different systems such as the heavy fermion systems or non-superconducting transition-metal compounds.
It should be noted that the electronic ordering states which are ubiquitous in correlated electron systems in principle are expected to be accompanied by a spin density wave, as is indicated in Fig. 17d. This magnetic superstructure has not yet been observed by STM/STS because this techniques *a priori* is not sensitive to magnetism. This changes, however, if a magnetic tunneling tip is used, a technique which has been explored and brought into maturity for non- or weakly correlated systems [63]. The experimental efforts to apply this spin-polarized scanning tunneling microscopy (SP-STM) to correlated electron systems have just started, yielding first exciting results [64]. One may stay tuned.

References

[1] J. Bardeen, Phys. Rev. Lett. **6**, 57 (1961)

[2] J. Tersoff and D.R. Hamann, Phys. Rev. Lett. **50**, 1998 (1983)

[3] J. Tersoff and D.R. Hamann, Phys. Rev. B **31**, 805 (1985)

[4] J.A. Strocio and W.J. Kaiser (Eds.): *Scanning Tunneling Microscopy* (Academic Press, Inc., 1993)

[5] R. Wiesendanger: *Scanning Probe Microscopy and Spectroscopy Methods and Applications* (Cambridge University Press, 1994)

[6] D.E. Moncton, J.D. Axe, and F.J. DiSalvo, Phys. Rev. Lett. **34**, 734 (1975)

[7] B.E. Brown and D.J. Beerntsen, Acta Crystallographica **18**, 31 (1965)

[8] R. Schlegel, T. Hänke, D. Baumann, M. Kaiser, P.K. Nag, R. Voigtländer, D. Lindackers, B. Büchner, and C. Hess, Review of Scientific Instruments **85**, 013706 (2014)

[9] J. Ziman: *Principles of the Theory of Solids* (Cambridge University Press, 1972)

[10] M.F. Crommie, C.P. Lutz, and D.M. Eigler, Nature **363**, 524 (1993)

[11] Y. Hasegawa and P. Avouris, Phys. Rev. Lett. **71**, 1071 (1993)

[12] P. Avouris, I. Lyo, R.E. Walkup, and Y. Hasegawa, Journal of Vacuum Science & Technology B **12**, 1447 (1994)

[13] L. Petersen, P.T. Sprunger, P. Hofmann, E. Lægsgaard, B.G. Briner, M. Doering, H.-P. Rust, A.M. Bradshaw, F. Besenbacher, and E.W. Plummer, Phys. Rev. B **57**, R6858 (1998)

[14] J.E. Hoffman, K. McElroy, D.-H. Lee, K.M. Lang, H. Eisaki, S. Uchida, and J.C. Davis, Science **297**, 1148 (2002)

[15] Y. Kamihara, T. Watanabe, M. Hirano, and H. Hosono, J. Am. Chem. Soc. **130**, 3296 (2008)

[16] D.C. Johnston, Advances in Physics **59**, 803 (2010)

[17] I.I. Mazin, D.J. Singh, M.D. Johannes, and M.H. Du, Phys. Rev. Lett. **101**, 057003 (2008)

[18] H. Eschrig, A. Lankau, and K. Koepernik, Phys. Rev. B **81**, 155447 (2010)

[19] X. Zhou, C. Ye, P. Cai, X. Wang, X. Chen, and Y. Wang, Phys. Rev. Lett. **106**, 087001 (2011)

[20] F. Massee, S. de Jong, Y. Huang, J. Kaas, E. van Heumen, J.B. Goedkoop, and M.S. Golden, Phys. Rev. B **80**, 140507 (2009)

[21] J.E. Hoffman, Reports on Progress in Physics **74**, 124513 (2011)

[22] T. Hänke, S. Sykora, R. Schlegel, D. Baumann, L. Harnagea, S. Wurmehl, M. Daghofer, B. Büchner, J. van den Brink, and C. Hess, Phys. Rev. Lett. **108**, 127001 (2012)

[23] T. Hanaguri, K. Kitagawa, K. Matsubayashi, Y. Mazaki, Y. Uwatoko, and H. Takagi, Phys. Rev. B **85**, 214505 (2012)

[24] S. Chi, S. Grothe, R. Liang, P. Dosanjh, W.N. Hardy, S.A. Burke, D.A. Bonn, and Y. Pennec, Phys. Rev. Lett. **109**, 087002 (2012)

[25] S. Grothe, S. Chi, P. Dosanjh, R. Liang, W.N. Hardy, S.A. Burke, D.A. Bonn, and Y. Pennec, Phys. Rev. B **86**, 174503 (2012)

[26] M.P. Allan, A.W. Rost, A.P. Mackenzie, Y. Xie, J.C. Davis, K. Kihou, C.H. Lee, A. Iyo, H. Eisaki, and T.-M. Chuang, Science **336**, 563 (2012)

[27] A. Lankau, K. Koepernik, S. Borisenko, V. Zabolotnyy, B. Büchner, J. van den Brink, and H. Eschrig, Phys. Rev. B **82**, 184518 (2010)

[28] J.H. Tapp, Z. Tang, B. Lv, K. Sasmal, B. Lorenz, P.C.W. Chu, and A.M. Guloy, Phys. Rev. B **78**, 060505 (2008)

[29] G. Binnig, H. Rohrer, C. Gerber, and E. Weibel, Phys. Rev. Lett. **49**, 57 (1982)

[30] I. Giaever, Phys. Rev. Lett. **5**, 147 (1960)

[31] I. Giaever, Phys. Rev. Lett. **5**, 464 (1960)

[32] J.M. Rowell, P.W. Anderson, and D.E. Thomas, Phys. Rev. Lett. **10**, 334 (1963)

[33] D.J. Scalapino, J.R. Schrieffer, and J.W. Wilkins, Phys. Rev. **148**, 263 (1966)

[34] J. Bardeen, L.N. Cooper, and J.R. Schrieffer, Phys. Rev. **108**, 1175 (1957)

[35] G.M. Eliashberg, JETP **11** (1960)

[36] P.K. Nag, R. Schlegel, D. Baumann, H.-J. Grafe, R. Beck, S. Wurmehl, B. Büchner, and C. Hess, Scientific Reports **6**, 27926 (2016)

[37] Y. Wang, A. Kreisel, V.B. Zabolotnyy, S.V. Borisenko, B. Büchner, T.A. Maier, P.J. Hirschfeld, and D.J. Scalapino, Phys. Rev. B **88**, 174516 (2013)

[38] N. Qureshi, P. Steffens, Y. Drees, A.C. Komarek, D. Lamago, Y. Sidis, L. Harnagea, H.-J. Grafe, S. Wurmehl, B. Büchner, and M. Braden, Phys. Rev. Lett. **108**, 117001 (2012)

[39] N. Qureshi, P. Steffens, D. Lamago, Y. Sidis, O. Sobolev, R.A. Ewings, L. Harnagea, S. Wurmehl, B. Büchner, and M. Braden, Phys. Rev. B **90**, 144503 (2014)

[40] J. Knolle, V.B. Zabolotnyy, I. Eremin, S.V. Borisenko, N. Qureshi, M. Braden, D.V. Evtushinsky, T.K. Kim, A.A. Kordyuk, S. Sykora, C. Hess, I.V. Morozov, S. Wurmehl, R. Moessner, and B. Büchner, Phys. Rev. B **86**, 174519 (2012)

[41] S.V. Borisenko, V.B. Zabolotnyy, D.V. Evtushinsky, T.K. Kim, I.V. Morozov, A.N. Yaresko, A.A. Kordyuk, G. Behr, A. Vasiliev, R. Follath, and B. Büchner, Phys. Rev. Lett. **105**, 067002 (2010)

[42] K. Umezawa, Y. Li, H. Miao, K. Nakayama, Z.-H. Liu, P. Richard, T. Sato, J.B. He, D.-M. Wang, G.F. Chen, H. Ding, T. Takahashi, and S.-C. Wang, Phys. Rev. Lett. **108**, 037002 (2012)

[43] S.V. Borisenko, V.B. Zabolotnyy, A.A. Kordyuk, D.V. Evtushinsky, T.K. Kim, I.V. Morozov, R. Follath, and B. Büchner, Symmetry **4**, 251 (2012)

[44] P. Hlobil, J. Jandke, W. Wulfhekel, and J. Schmalian, arXiv:1603.05288 (2016)

[45] Y. Wang, P.J. Hirschfeld, and I. Vekhter, Phys. Rev. B **85**, 020506 (2012)

[46] C. Hess, S. Sykora, T. Hänke, R. Schlegel, D. Baumann, V.B. Zabolotnyy, L. Harnagea, S. Wurmehl, J. van den Brink, and B. Büchner, Phys. Rev. Lett. **110**, 017006 (2013)

[47] S. Chi, S. Johnston, G. Levy, S. Grothe, R. Szedlak, B. Ludbrook, R. Liang, P. Dosanjh, S.A. Burke, A. Damascelli, D.A. Bonn, W.N. Hardy, and Y. Pennec, Phys. Rev. B **89**, 104522 (2014)

[48] P.M.R. Brydon, M. Daghofer, C. Timm, and J. van den Brink, Phys. Rev. B **83**, 060501 (2011)

[49] A.A. Kordyuk, V.B. Zabolotnyy, D.V. Evtushinsky, T.K. Kim, I.V. Morozov, M.L. Kulic, R. Follath, G. Behr, B. Büchner, and S.V. Borisenko, Phys. Rev. B **83**, 134513 (2011)

[50] B. Zeng, D. Watanabe, Q.R. Zhang, G. Li, T. Besara, T. Siegrist, L.Y. Xing, X.C. Wang, C.Q. Jin, P. Goswami, M.D. Johannes, and L. Balicas, Phys. Rev. B **88**, 144518 (2013)

[51] M. Tinkham: *Introduction to Superconductivity* (McGraw-Hill, 1996)

[52] T. Hanaguri, Y. Kohsaka, M. Ono, M. Maltseva, P. Coleman, I. Yamada, M. Azuma, M. Takano, K. Ohishi, and H. Takagi, Science **323**, 923 (2009)

[53] T. Hanaguri, S. Niitaka, K. Kuroki, and H. Takagi, Science **328**, 474 (2010)

[54] P.J. Hirschfeld, D. Altenfeld, I. Eremin, and I.I. Mazin, Phys. Rev. B **92**, 184513 (2015)

[55] P.A. Lee, N. Nagaosa, and X.-G. Wen, Rev. Mod. Phys. **78**, 17 (2006)

[56] K. McElroy, R.W. Simmonds, J.E. Hoffman, D.-H. Lee, J. Orenstein, H. Eisaki, S. Uchida, and J.C. Davis, Nature **422**, 592 (2003)

[57] Q.-H. Wang and D.-H. Lee, Phys. Rev. B **67**, 020511 (2003)

[58] O. Fischer, M. Kugler, I. Maggio-Aprile, C. Berthod, and C. Renner, Rev. Mod. Phys. **79**, 353 (2007)

[59] T. Hanaguri, C. Lupien, Y. Kohsaka, D.-H. Lee, M. Azuma, M. Takano, H. Takagi, and J.C. Davis, Nature **430**, 1001 (2004)

[60] J.E. Hoffman, E.W. Hudson, K.M. Lang, V. Madhavan, H. Eisaki, S. Uchida, and J.C. Davis, Science **295**, 466 (2002)

[61] J.C.S. Davis and D.-H. Lee, Proceedings of the National Academy of Sciences **110**, 17623 (2013)

[62] E. Fradkin and S.A. Kivelson, Nat Phys **8**, 864 (2012)

[63] R. Wiesendanger, Rev. Mod. Phys. **81**, 1495 (2009)

[64] M. Enayat, Z. Sun, U.R. Singh, R. Aluru, S. Schmaus, A. Yaresko, Y. Liu, C. Lin, V. Tsurkan, A. Loidl, J. Deisenhofer, and P. Wahl, Science **345**, 653 (2014)